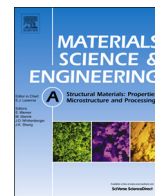




ELSEVIER

Contents lists available at ScienceDirect

## Materials Science &amp; Engineering A

journal homepage: [www.elsevier.com/locate/msea](http://www.elsevier.com/locate/msea)

## Texture, anisotropy in microstructure and mechanical properties of IN738LC alloy processed by selective laser melting (SLM)

Karsten Kunze<sup>a,\*</sup>, Thomas Etter<sup>b</sup>, Jürgen Grässlin<sup>c</sup>, Valery Shklover<sup>c</sup><sup>a</sup> Scientific Center of Optical and Electron Microscopy (ScopeM), ETH Zürich, CH-8093 Zürich, Switzerland<sup>b</sup> ALSTOM (Switzerland) Ltd., CH-5401 Baden, Switzerland<sup>c</sup> Laboratory of Crystallography, Department of Materials, ETH Zürich, CH-8093 Zürich, Switzerland

## ARTICLE INFO

## Article history:

Received 17 July 2014

Received in revised form

30 September 2014

Accepted 1 October 2014

Available online 14 October 2014

## Keywords:

Nickel based superalloys

Selective laser melting (SLM)

Electron backscatter diffraction (EBSD)

X-ray diffraction

Texture

Mechanical characterization

## ABSTRACT

Nickel-based IN738LC samples were built by selective laser melting (SLM). To evaluate the anisotropic mechanical behavior of IN738LC material due to layer-wise build up, specimens were built with their cylinder axis (loading direction) oriented either parallel to the building direction, or perpendicular to the building direction and at 45° to the laser scanning direction. After building up the specimens by SLM, they were investigated either under the 'as-built' condition or after heat treatment and compared to IN738LC cast material. The analysis of microstructural anisotropy in SLM made IN738LC specimens was done by using EBSD, EDX and X-ray texture analysis methods, and then correlated with anisotropic material behavior observed during tensile and creep testing at room temperature and 850 °C. All SLM samples possess the same general texture, with the majority of grains forming one single component of a cube texture with one of the cubic axes parallel to the building direction, and another cubic axis parallel to the laser scanning direction. The Young's modulus determined during tensile testing is significantly lower parallel to the building direction than perpendicular to the building direction, with the values for cast IN738LC material in between. Creep behavior of specimens with loading parallel to the building direction is superior compared to specimens with loading axis normal to the building direction. The anisotropy of Young's modulus was modeled based on the single crystal elastic tensor and the measured crystallographic preferred orientations, and compares well with the data from tensile tests.

© 2014 Elsevier B.V. All rights reserved.

## 1. Introduction

Ni-base superalloys are extensively used for turbine blades and vanes in aero- and industrial gas turbine engines. The mechanical properties of Ni-base superalloys depend on the grain structure, dendrite arm spacing,  $\gamma'$  volume fraction,  $\gamma/\gamma'$  eutectic and various types of secondary phases, such as carbides and borides; see for instance [1,2]. The Ni-base superalloy IN738LC has been widely used in today's heavy-duty gas turbines for hot gas path components such as blades, vanes and heat shields [3]. It is a  $\gamma'$  precipitation-strengthened superalloy and possesses a good combination of high-temperature strength and oxidation resistance. The unique mechanical properties of the IN738LC superalloy are due to the hardening of a fcc  $\gamma$ -Ni matrix by solid-solution strengthening and fine precipitates. Like many other Ni-base superalloys, IN738LC alloy is strengthened mainly through the precipitation of the  $\gamma'$  phase having Ni<sub>3</sub>(Al, Ti) basic composition and L1<sub>2</sub> crystal structure [4]. Heat treatment of IN738LC alloy

affects the size, shape and fraction of  $\gamma'$  precipitates in the matrix and consequently affects the mechanical properties. The influence of different heat treatments on the microstructure of polycrystalline IN738LC alloy is reported for instance in [5]. The morphology of  $\gamma'$  in IN738LC alloy is also affected by the cooling rate from heat treatment to room temperature [6]. Because of its alloying constituents and high  $\gamma'$  volume fraction leading to a substantial hot cracking sensitivity, IN738LC material is very difficult to weld [7–11].

The progress in superalloy performance would not be possible without the parallel improvement of processing technology [1]. In this study we apply selective laser melting (SLM), which can be used to produce directly metallic parts from powder materials. Thin powder layers with a typical thickness of 20–60  $\mu\text{m}$  are generated on a metallic base plate or the already produced skeleton of a designed object [12]. The cross-sections of a sliced CAD file are scanned subsequently using a high power laser beam in order to melt the powder material. Additive manufacturing processes such as SLM (see, for example [13,14]) are prospective candidates to complement or replace conventional machining/production processes such as cutting or casting. Due to powder based article production and the inherently high impact rates of

\* Corresponding author.

E-mail address: [karsten.kunze@scopem.ethz.ch](mailto:karsten.kunze@scopem.ethz.ch) (K. Kunze).

the laser beam-material interaction in these processes, the resulted material is very homogeneous with respect to chemical composition and principally free of segregations and residual eutectic inclusions [15].

So far, few nickel-based superalloys have been processed by SLM, among them Hastelloy X [16], IN718 [17] or Waspaloy [18]. Their  $\gamma'$  volume fraction is lower compared to IN738LC. The high susceptibility to cracking of precipitation hardenable nickel-based superalloy CM247LC is reported in [19].

The high thermal gradients in SLM processing cause crystals to grow preferentially in well-defined directions, resulting in specific microstructures and textures [20]. Suitable scanning strategies may favor either sharp single component textures or more uniformly distributed crystal orientations [20]. The anisotropy of mechanical properties is largely controlled by the texture and can be modeled based on the texture and the single crystal mechanical properties [21,22].

As it has been shown in [15], SLM made IN738LC specimens with a porosity content of <0.5% could be produced without macro-cracking and showed promising mechanical properties. The aim of the present study is the analysis of microstructural anisotropy in SLM made IN738LC specimens using EBSD, EDX and X-ray texture analysis methods, and its correlation with anisotropic material behavior observed during mechanical testing.

## 2. Experimental

The IN738LC alloy powder, produced by gas atomizing virgin cast material, was obtained from Nanoval (Germany, [www.nanoval.de](http://www.nanoval.de)). The powder has a particle size of 325 mesh and a nominal weight percentage composition of 15.88% Cr, 8.30% Co, 1.75% Mo, 2.62% W, 1.9% Ta, 0.90% Nb, 3.51% Al, 3.31% Ti, 0.10% C, 0.011% B, and Ni (balance).

A “Concept LaserCusing M1” SLM machine (ES Technology Ltd., UK, [www.estechology.net](http://www.estechology.net)) [12], kindly made available through inspire AG (ETH Zürich, Switzerland, [www.inspire.ethz.ch](http://www.inspire.ethz.ch)) was used to build specimens with their cylinder axis oriented either parallel or perpendicular to the building direction, as shown in

**Fig. 1.** The Z-axis of the specimen is defined parallel to the building direction, whereas each layer is deposited parallel to the XY-plane with the laser scanning at 45° between X and Y. After building up the specimens by SLM, they were cut from the substrate plate by electro-discharge machining. As listed in Table 1, samples were investigated either under the ‘as-built’ condition or after heat treatment, which included hot isostatic pressing (HIP, at 1180 °C for 4 h), standard solution (SHT, at 1120 °C for 2 h) and precipitation hardening (PHT, at 850 °C for 20 h) heat treatment. All specimens for mechanical testing were heat-treated and then machined to their end contour.

Tensile testing at ambient and elevated temperature (850 °C) of M10 specimens were carried out with a 50 kN load cell at a strain rate of ~4%/min. The specimens were heated in a resistance furnace. Test were performed after reaching the testing temperature with a hold time of ~30 min. At least two specimens for each condition were tested.

In addition to tensile testing, creep tests were performed at 850 °C. The creep behavior of SLM-machined specimens has been compared to fully heat-treated IN738LC cast material. Of special interest was the stress level for 1% total strain. Further details about the equipment used for mechanical testing are documented in [15].

Specific section cuts for microstructural characterization of different samples are defined in Fig. 1 and Table 1. Grinding of the specimens for metallurgical analysis was started with 150 grit disk (corundum) followed by polishing with 15  $\mu\text{m}$ , 9  $\mu\text{m}$ , 6  $\mu\text{m}$ , 3  $\mu\text{m}$ , and 1  $\mu\text{m}$  diamond suspension. In order to reveal the grain size and morphology, the specimens were etched in Adler reagent (50 ml H<sub>2</sub>O, 100 ml HCl, 30 g FeCl<sub>3</sub>, 6 g (NH<sub>4</sub>)<sub>2</sub>[CuCl<sub>4</sub>]<sub>2</sub>) for few seconds. A Polyvar MET light microscope from Reichert-Jung was used for metallographic analysis.

XRD patterns were obtained using an X'Pert Pro X-ray powder diffractometer (PANalytical, Almelo, The Netherlands) with CuK $\alpha$  radiation ( $\lambda=1.54056 \text{ \AA}$ ). Diffraction patterns were recorded within the  $2\theta$  range from 10° to 90° using standard  $\theta$ - $2\theta$  Bragg-Brentano geometry. The X-ray beam was collimated to a spot size of 3 mm in diameter on the sample surface. Pole figures of all samples are measured in reflection mode using the same

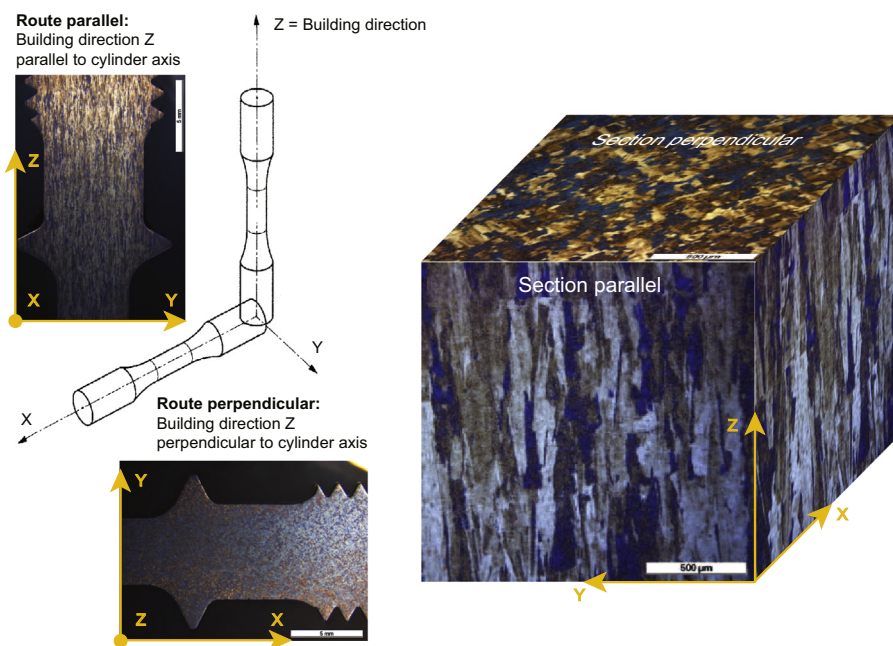


**Fig. 1.** Schematic drawing of SLM building direction, grain shape preferred orientation and cylinder axis of the test specimen with respect to a common specimen fixed reference frame XYZ.

diffractometer equipped with a Eulerian cradle in  $3^\circ$  steps for both  $\phi$  and  $\psi$ , with  $0 < \psi < 75^\circ$  and  $0 < \phi < 360^\circ$ , at  $2\theta$  angle of  $43.8^\circ$  for (111),  $51.0^\circ$  for (200) and  $74.9^\circ$  for (220), respectively. Complete pole figures were re-calculated from an orientation density function (ODF), which was estimated from the measured incomplete pole figures using pole figure inversion routines [23] implemented in the MTEX [24] MATLAB toolbox (<http://code.google.com/p/mtex/>).

For texture analysis by SEM-based electron back scatter diffraction (EBSD), the surface of the samples was ultra-polished with MasterMet<sup>®</sup> 2 non-crystallizing colloidal silica polishing suspension (Buehler, U.S.A., [www.buehler.com](http://www.buehler.com), suspension Identification Number 40-6380-064). The texture analysis was performed on a field emission SEM Quanta 200F (FEI, U.S.A., [www.fei.com](http://www.fei.com)) equipped with a Hikari EBSD module and software package OIM 5.2 (EDAX, U.S.A., [www.edax.com](http://www.edax.com)). EBSD data acquisition was

carried out at 20 kV acceleration voltage, 15 mm working distance, 40  $\mu\text{m}$  aperture and a spot size of 5, resulting in a nominal beam current of 7 nA. Raw data were gently post-processed for rendering orientation maps. Only reliable data (confidence index  $> 0.1$ ) were used for texture representation and subsequent modeling.

Hyperspectral element mappings were performed on the polished sample surfaces using the FEI Quanta 200F SEM equipped with a SDD-EDX detector EDAX Apollo X, operated at an accelerating voltage of 10 kV and a beam current of 12 nA. The raw data collected on a raster of 256 by 200 pixels were post processed to calculate semi-quantitative mappings of element concentrations in order to suppress artifacts due to peak overlaps. Electron probe micro-analysis was performed using a JXA-8200 instrument (JEOL, Japan, [www.jeol.co.jp/en](http://www.jeol.co.jp/en)) at the Earth science department of ETH Zurich, operated at an accelerating voltage of 15 kV and a beam current of 20 nA.

**Table 1**

Thermal history and Young's modulus of investigated IN738LC samples (SLM and reference cast material).

Processing	SLM without HT	SLM with HT	Cast with HT		
Heat treatment (HT)		HIP (1180 °C/4 h)+1120 °C/2 h+850 °C/20 h	1120 °C/2 h+850 °C/20 h		
<b>Microstructural characterization</b>					
Specimen shape	Cube	Cylinder	Cylinder		
Section plane XY perpendicular to building direction Z	Sample no. 10	Sample no. 2s			
Section plane YZ parallel to building direction Z	Sample no. 9	Sample nos. 1, 2			
Section cut in arbitrary orientation			Sample no. 3		
<b>Young's modulus in GPa</b>		<b>At RT (23 °C)</b>	<b>At 850 °C</b>	<b>At RT (23 °C)</b>	<b>At 850 °C</b>
<i>Tensile testing</i>					
Testing direction perpendicular to building direction Z		237 ± 7 (2 specimens)	159 ± 4 (4 specimens)		
Testing direction parallel to building direction Z		158 ± 3 (3 specimens)	110 ± 2 (5 specimens)		
Testing direction arbitrary (ALSTOM material database)				200	144
<i>Texture-based predictions (Reuss-Voigt bounds)</i>					
Parallel X or Y		208–240	152–175		
Parallel Z		147–177	108–129		
Parallel X+Y or X–Y		144–173	106–126		
Parallel $\pm 1.4 \times X \pm Z$		244–274	176–199		
Any direction (uniform texture)				188–233	138–170

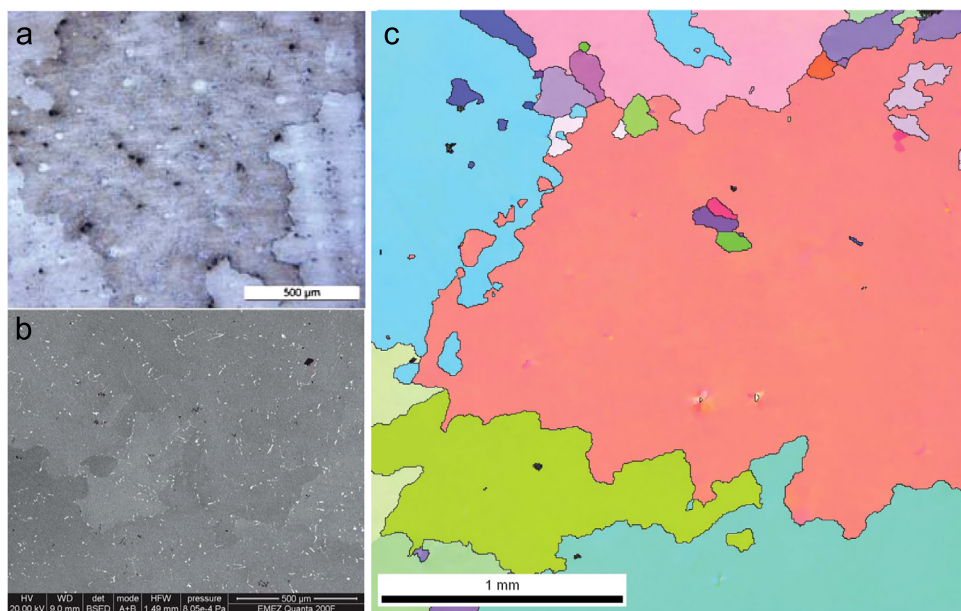


**Fig. 2.** Grain microstructure and precipitates in IN738LC cast material (sample 3). Light optical image (a), SEM backscatter electron (BSE) image (b) and orientation map (c) using the standard IPF color key with respect to an arbitrary reference direction. Black line segments indicate traces of high angle grain boundary (defined by  $> 15^\circ$  misorientation between neighbor pixels). (For interpretation of the references to color in this figure legend, the reader is referred to the web version of this article.)

### 3. Results

#### 3.1. Microstructure

A remarkable correlation of the solidification morphology of IN738LC grains with the SLM building direction can be seen from Fig. 1. The grains are primarily aligned in a distinct columnar structure along the building axis with a grain shape aspect ratio of 1:10 or higher, comparable to a directionally solidified microstructure. Section cuts perpendicular to the building direction show a ‘chessboard’ microstructure with rather equiaxed grain shapes, but preferential alignment of grain boundaries at about  $45^\circ$  with respect to the XY directions defined by the SLM process. Note that the columnar grains along the Z-direction are not restricted to one laser bead but extend into adjacent layers showing that crystallographic orientations are epitaxially inherited from prior solidified grains. The grain long axes approach the mm-range, which is clearly larger than a powder layer with a typical thickness of 20–60  $\mu\text{m}$ .

From light optical estimation, the grain size in SLM specimen is about millimeters in the long axis (along the building direction) and about 0.1 mm in the shorter two axes (perpendicular to the building direction), which is much smaller than the grain size in cast material ranging between millimeter and centimeter. The grain and precipitate distribution in IN738LC cast material is characterized by an optical metallographic image (Fig. 2a), a SEM BSE image (Fig. 2b) and an orientation map (Fig. 2c), all at the same scale with mm-sized field of view.

The light optical observations are verified in orientation maps derived from EBSD scans (Fig. 3). Section cuts parallel to the building direction confirm the columnar grain morphology, and sections cuts perpendicular to the building direction validate a

‘chessboard’ microstructure with preferentially aligned grain boundaries at about  $45^\circ$  to the X and Y axes. All maps reveal a vast amount of orientation gradients and small angle boundaries within the grains (visible as subtle variation in color), separated by large angle boundaries (visible by black line segments). The preference of red color in the maps indicates a dominance of crystals aligned with one of their  $\langle 001 \rangle$  axes towards the building direction Z.

#### 3.2. Phase identification

The  $\gamma/\gamma'$  microstructure of the as-cast material (sample 3) is compared with the SLM samples without HT (sample 10) and with HT (sample 2) by means of SEM BSE images (Fig. 4) and EDX element maps (Fig. 5). The cast and heat treated samples can be described as having duplex-size  $\gamma'$  microstructure, the size of finer  $\gamma'$  precipitates roughly estimated as  $\sim 100$  nm, the size of coarser  $\gamma'$  precipitates is  $\sim 1$   $\mu\text{m}$ . Some of the  $\gamma'$  precipitates are cuboidal, others have irregular shape. No  $\gamma'$  precipitates were observed in SLM samples without HT (sample 10) at the finest available SEM resolution, i.e., above a size of a few tens nanometer.

Neither diffraction technique (XRD or EBSD) resolved any crystallographic misorientation between  $\gamma'$  precipitates and their  $\gamma$  host matrix, indicating seamless coherency (in line with almost identical lattice parameters) of the  $\gamma$ -Ni matrix phase (space group  $Fm\bar{3}m$ ) and the  $\gamma'$ -Ni<sub>3</sub>(Al, Ti) precipitate (space group  $Pm\bar{3}m$ ). The crystallite sizes (we cannot differentiate between  $\gamma$  and  $\gamma'$ ), determined from XRD peak broadening with the Scherrer formula, vary in a narrow range of 22–31 nm, which are significantly smaller than the size of even fine  $\gamma'$  precipitates visible on SEM images. The  $\gamma'$  precipitates are enriched in Ni, Ti, (Ta), and depleted in Cr, Co, (Mo) relative to the  $\gamma$  matrix. Rather homogeneous

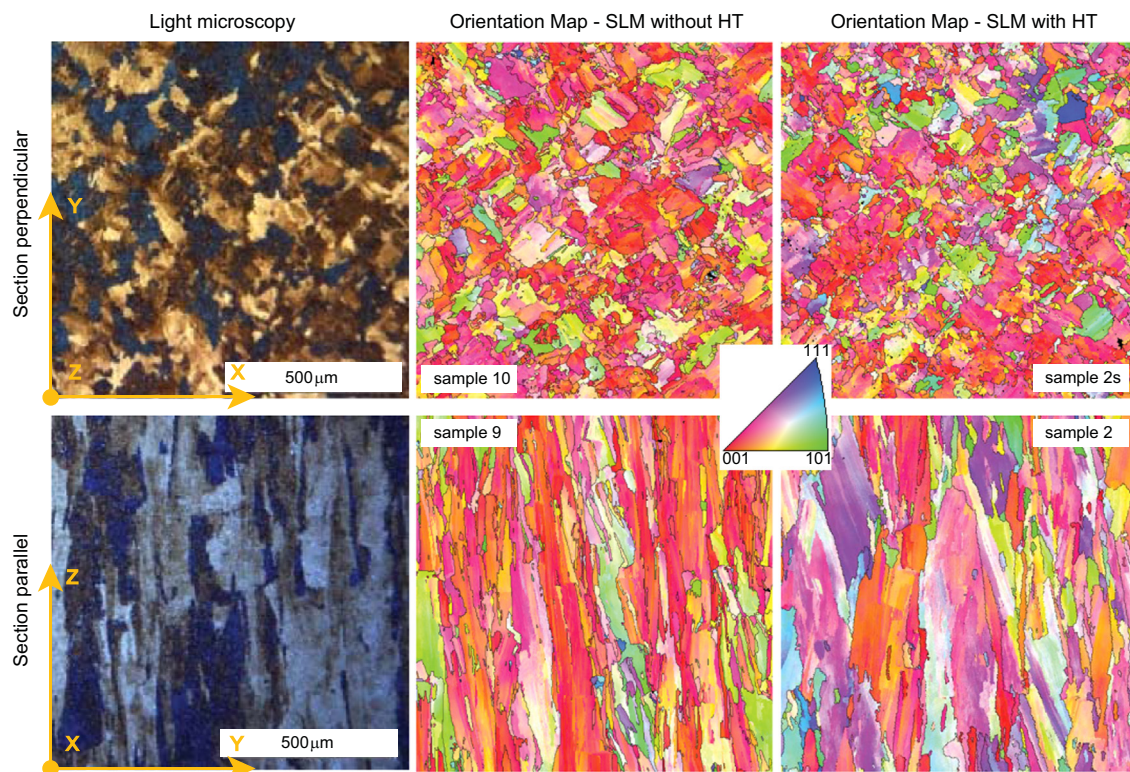


**Fig. 3.** Optical micrographs in etched condition and orientation maps derived from EBSD scans of SLM specimens. Specimen cut in sections perpendicular (top row) and parallel (bottom row) to the building direction. Samples are investigated in the ‘as built’ condition and after subsequent heat treatment. All orientation maps are colored using the standard IPF color key with respect to the building direction Z. Black line segments indicate traces of high angle grain boundary (defined by  $> 15^\circ$  misorientation between nearest neighbor pixels). (For interpretation of the references to color in this figure legend, the reader is referred to the web version of this article.)

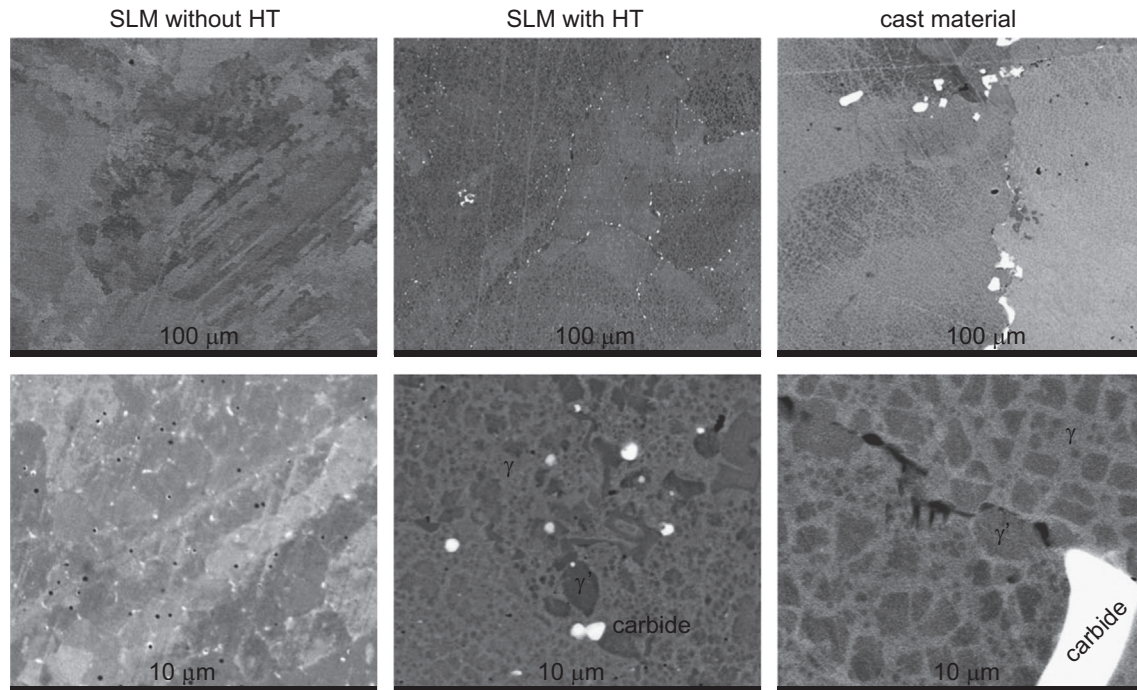


**Fig. 4.** Precipitates in IN738LC specimen as visualized by SEM backscatter electron (BSE) images at two different magnifications for SLM without HT (sample 10, left), SLM with HT (sample 2, center), cast material (sample 3, right). Grain orientation contrast and composition contrast of  $\gamma'$  and  $\gamma$  phases are visible at various gray levels, heavy metal carbides are displayed by very bright levels.

distributions are observed for W. Using electron probe micro-analysis, admittedly limited by the small size of  $\gamma'$ -Ni<sub>3</sub>(Al, Ti)-precipitates, the Cr-content in the alloys varies from 15.1 to 21.1 at% for  $\gamma$ -phase and from 10.1 to 16.1 at% for the  $\gamma'$ -phase in different locations of the three samples. The XRD spectra of the cast specimen show signatures of diffuse X-ray scattering (Fig. 6b), considered as a result of destruction of ordered phases and formation of atomic short-range order (SRO) in cast alloy [25].

While cast material (sample 3) and heat-treated SLM samples (sample 2) show rather similar  $\gamma/\gamma'$  microstructures, they differ significantly in size and distribution of carbide precipitates (bright levels in Fig. 4). As carbides are preferentially distributed along grain boundaries, the finer grain size in SLM material correlates with a more dispersed and finer carbide distribution. Significantly less and extremely small carbide precipitates were observed in BSE images of SLM material without HT (sample 10) as compared to that after heat treatment (sample 2). Various precipitate phases are indicated by a series of minor peaks in the XRD spectra (Fig. 6b) as well as by EDX and microprobe analysis. Given the limitations in spatial resolution of the microanalysis applied, we infer predominantly stable cubic MC precipitates rich in M=(Ti, Nb, Ta). The color overlay images in Fig. 5 result from mixing C (red), Cr (green) and Ni (blue) and show about five different phases:  $\gamma$ -phase (brighter blue),  $\gamma'$ -phase (darker blue), carbides (red), Cr-rich carbide (yellow) and metallic Cr-enrichments (green). No separate phases are distinguishable from the element mapping on SLM material without HT (sample 10), though the map for Ti indicates some faint correlation of Ti enrichment with the bright nanoscale precipitates in the corresponding BSE image above in Fig. 5.

### 3.3. Texture analysis

The local and volume texture of the SLM samples is characterized by contoured pole densities, i.e., pole figures, as derived from EBSD scans as well as from XRD goniometry (Figs. 7 and 8). All

SLM samples possess the same general texture, represented by one single component of a cube texture rotated by 45° about the building direction. The majority of grains are oriented with some scatter around this preferred orientation, also characterized by  $\langle 001 \rangle \parallel Z$  and  $\langle 011 \rangle \parallel X$  and  $\langle 011 \rangle \parallel Y$ . The diagonal alignment of the grains is best reflected in the inverse pole figure with respect to the diagonal specimen direction  $X+Y$ , which shows again a strong preference of  $\langle 001 \rangle$  similarly to the inverse pole figure for the Z-direction (Fig. 7). Small deviations of the pole figure maxima from a perfectly symmetric pattern are due to experimental inaccuracy in cutting and mounting.

### 3.4. Tensile testing and creep behavior

Details about the tensile test results of SLM specimens built in two directions and comparison with cast material have been reported elsewhere [15]. The mechanical properties of the cast material (fully heat-treated, including solution and precipitation heat treatment) were used as a baseline. It has been shown that the yield strength of SLM specimens is significantly lower along the building direction (Z-specimen) than perpendicular to the building direction (XY-specimen). At room temperature the SLM specimen always had higher strength than cast material, while less striking differences were observed at elevated temperature (850 °C).

The anisotropy of mechanical properties of the SLM specimens is also reflected in measurements of Young's modulus at room and elevated temperature, as can be seen from Table 1, which lists the values of Young's modulus of the SLM specimens in comparison to reference data from Alstom's Material Database on cast IN738LC alloy. The Young's modulus as determined during tensile testing is significantly lower parallel to the building direction (Z-specimen) than perpendicular to the building direction (XY-specimen), with the values for (nominally isotropic) cast material between both extremes.

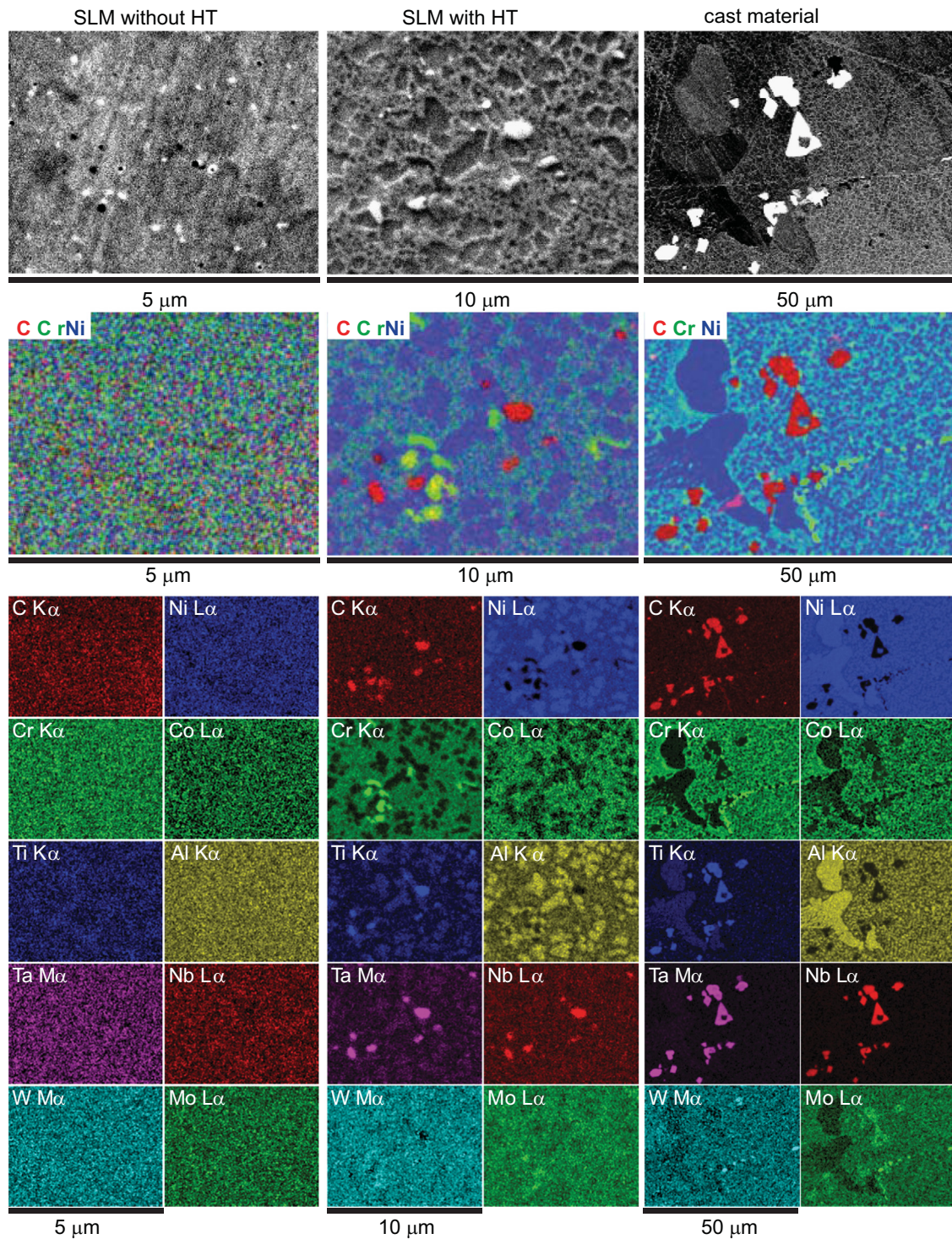


**Fig. 5.** Precipitates in IN738LC specimen as visualized by SEM–EDX element mapping at suitable magnifications for SLM without HT (sample 10, left), SLM with HT (sample 2, center), cast material (sample 3, right). SEM images (top), color overlay of element maps for C, Cr, Ni (middle), and element maps showing relative weight concentrations derived from hyperspectral mapping (bottom). Phases are distinguishable in the color overlay maps (second row) for SLM with HT and for cast material by bright blue ( $\gamma$ ), dark blue ( $\gamma'$ ), red (carbides) as well as yellow-green (Cr rich components) colors. (For interpretation of the references to color in this figure legend, the reader is referred to the web version of this article.)

**Fig. 9** compares the time to reach 1% total strain for different stress levels at 850 °C. As can be seen from these creep tests, the Z-specimens have superior creep properties compared to the XY-specimens, but slightly inferior compared to cast IN738LC. The SLM specimens have in general lower creep rupture strengths than cast material, with the Z-specimens still in the lower scatter band of cast material [15].

## 4. Discussion

### 4.1. Microstructure

The specimens built by SLM show a significant anisotropy in microstructure, texture and mechanical behavior. Pronounced grain shape anisotropy is immediately obvious from microscopic

observations, with the grain long axis aligned with the building direction Z. However, the observed anisotropy in mechanical properties is not primarily correlated to grain shape, but is first of all explained with the texture, i.e., crystallographic preferred orientation, of the material, as detailed below.

#### 4.2. Phase identification

The cubic lattice constants in studied IN738LC samples (which can be related to both  $\gamma$  and  $\gamma'$ ) lie in a range of 3.587(1)–3.598(3)Å, what is larger than the 3.567 Å in Ni<sub>3</sub>Al [26]. The alloying elements substitute for both Ni and X in Ni<sub>3</sub>X alloys, both substitution of Ni by

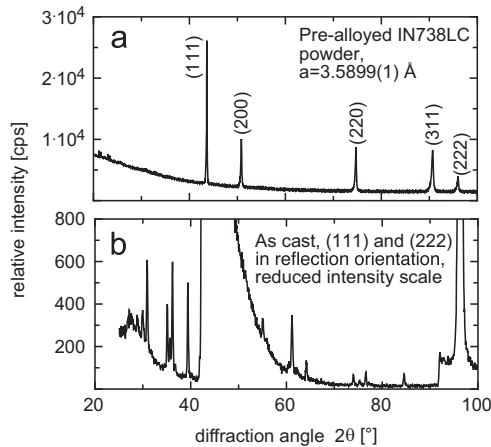


**Fig. 6.** XRD spectra of IN738LC. (a) Raw powder used for the SLM process. (b) Cast material (sample 3), with planes (111) and (222) in reflecting position. Intensity scale is reduced to show presence of minor peaks. Peak shape of (111) shows signature of diffuse X-ray scattering. Additional peaks indicate secondary (minor) phases in cast alloy inferred as carbide precipitates.

Co, Fe, Cr, Mo, W and substitution of Al by Ti or Nb lead to increase of the lattice parameters [26]. Major part of Cr and Mo remains in the matrix, but Cr and Mo can substitute for both Al and Ni in Ni<sub>3</sub>X [26].

An almost zero misfit of the  $\gamma$  and  $\gamma'$  phases in studied IN738LC samples can be assumed, as it was stated in previous studies of IN738LC alloy, indicating a small misfit of 0.17–0.36% [27]. Fine dispersion of  $\gamma'$ -Ni<sub>3</sub>(Ti, Al) precipitates in the  $\gamma$ -Ni matrix and full coherency of  $\gamma/\gamma'$  interfaces (misfit 0–0.2%), allowing a fine superalloy structure to maintain at high temperature, explain also the high strength of heat-resistant nimonic alloys [28, p. 298]. As it is emphasized in [28], the total creep-rupture of nimonic alloys can be remarkably increased by a factor of 50 by directional control of alloy composition to reduce the misfit further below the 0.2% misfit.

The observed SRO effect is usually associated with Cr and appears to be much higher in the  $\gamma$  phase than in  $\gamma'$  [1]. SRO in transition metal alloys, forming solid solution, influences physical properties of these alloys mainly through the influence on the dislocation movement, for example, SRO explains anomalies in concentration dependence of specific heat and elastic behavior [25]. The simultaneous occurrences of SRO, precipitation hardening and long range order in the  $\gamma$  phase are called to be reason for property change of superalloys.

#### 4.3. Texture analysis

All investigated SLM samples possess the same type of a single component texture. Small differences in the texture between different SLM samples and between EBSD and XRD techniques are within grain counting statistics and should not be interpreted. Depending on the number of grains covered by the respective measurements, the pole figures resemble some signatures of a small finite number of individual grains rather than a smooth

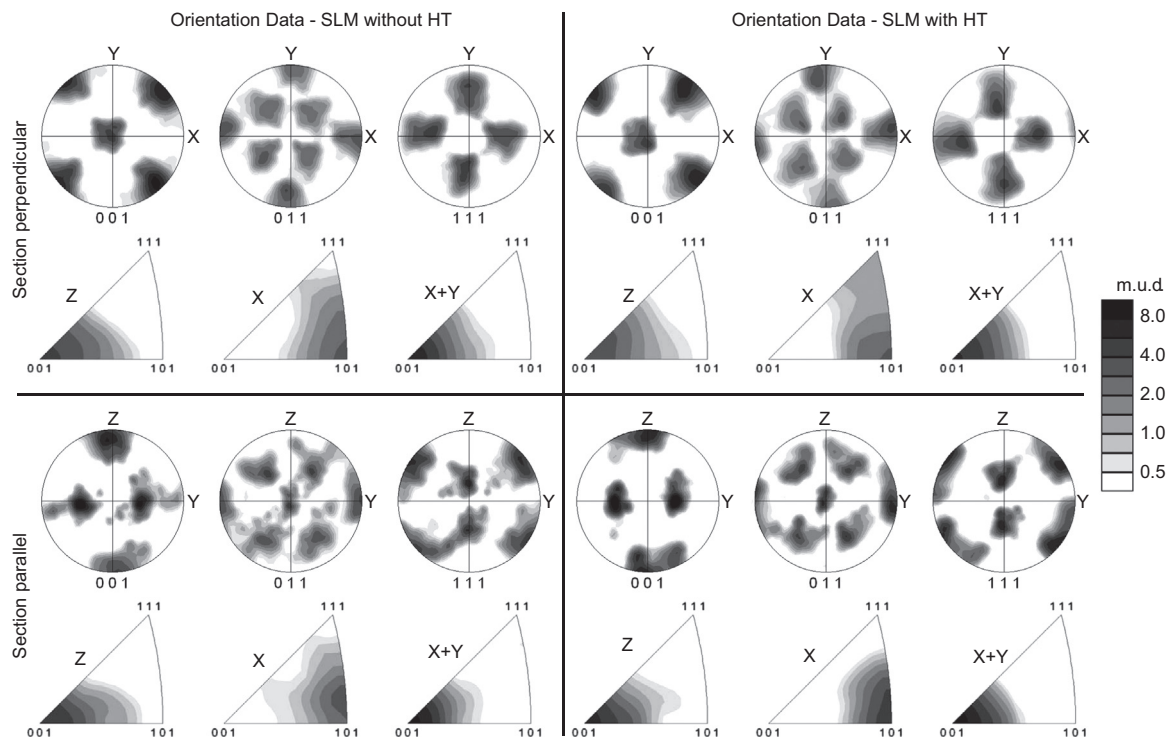


**Fig. 7.** Crystal preferred orientation obtained by EBSD, represented as pole figures 001, 011, 111 and as inverse pole figures with respect to the building direction Z as well as the X and the X+Y directions. Specimen cut in sections perpendicular (top row) and parallel (bottom row) to the building direction. Samples processed by SLM ‘as built’ or with subsequent heat treatment. Sample numbers refer to 10 (top left), 2 s (top right), 9 (bottom left), 2 (bottom right). Legend key indicates contour levels in multiples of uniform distribution (m.u.d.) after smoothing the individual orientation data by Gaussian convolution with 5° width using harmonic calculus up to  $L_{max}=34$ .

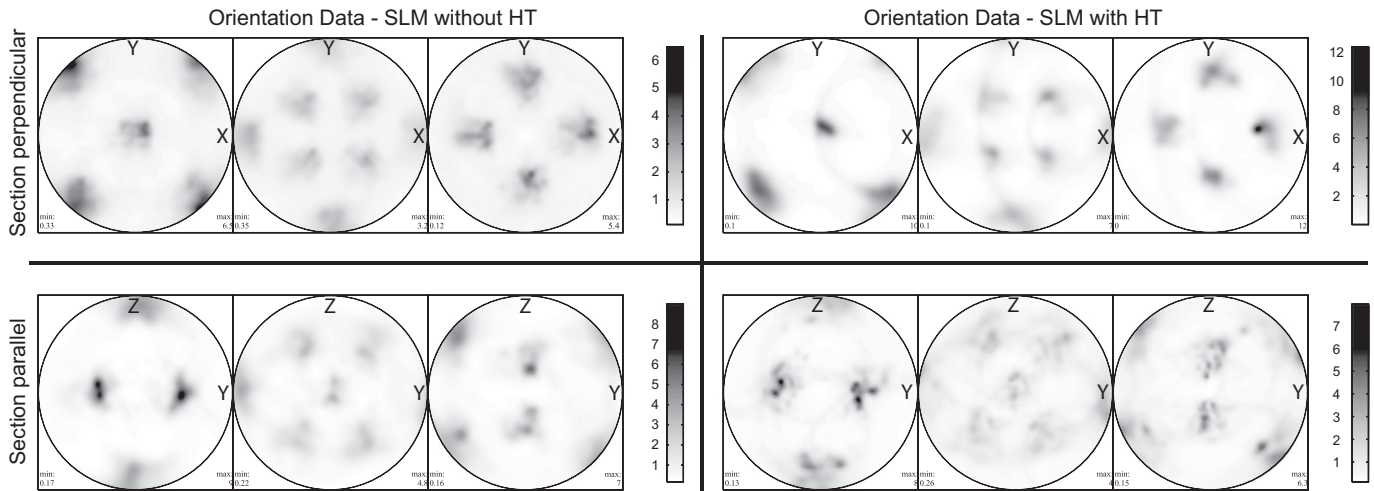


**Fig. 8.** Crystal preferred orientation obtained by XRD goniometry, represented as pole figures 001, 011 and 111. Specimen cut in sections perpendicular (top row) and parallel (bottom row) to the building direction. Samples processed by SLM 'as built' or with subsequent heat treatment. Sample numbers refer to 10 (top left), 2 s (top right), 9 (bottom left), 2 (bottom right). Legend keys indicate contour levels in multiples of uniform distribution (m.u.d.). Complete pole figures were re-calculated after ODF estimation from the incomplete pole figure data measured in reflection mode.

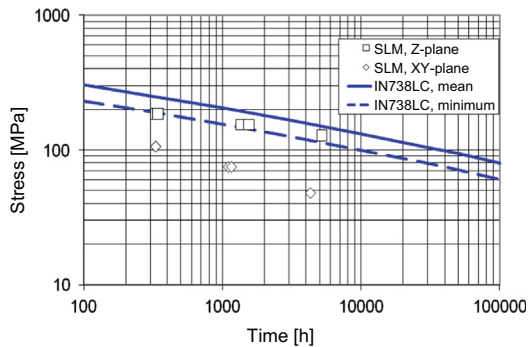


**Fig. 9.** Creep tests performed at 850 °C. Stress versus time to reach 1% total plastic strain: comparison between SLM processed specimens and cast IN738LC.

orientation density distribution. We selected the data set for SLM sample 10 without HT as a representative texture for subsequent discussion.

In the process of directional solidification, crystal alignment is controlled by one special direction, namely the normal to the solidification front or growth direction. Crystal orientations develop with  $\langle 100 \rangle$  preferentially aligned parallel to Z, but with random orientation around this single axis, resulting in rotationally symmetric preferred orientations, characterized as fiber texture  $\langle 100 \rangle \parallel Z$ . In the SLM process, two mutually perpendicular sample directions are controlling crystal alignment of the cubic  $\langle 100 \rangle$  axes, namely parallel to the building direction Z and to the laser scanning direction within the XY plane, respectively. As a result, the texture approaches a single component that is occupied by the majority of grains with some scatter and tolerance in the range of ten degrees.

#### 4.4. Anisotropy of mechanical properties

Single crystal elastic constants ( $c_{11}=235.16$  GPa,  $c_{12}=147.67$  GPa, and  $c_{44}=122.53$  GPa) of IN738LC [29] were used to represent the anisotropy of Young's modulus. The directional variation of Young's modulus for a single crystal is indicated in a three-dimensional representation as well as in a stereographic projection (Fig. 10a and b), with a minimum of 121 GPa along the crystal axes  $\langle 100 \rangle$  and a maximum of 299 GPa along the diagonal directions  $\langle 111 \rangle$ .

Texture based lower and upper bounds, also referred to as Reuss respectively Voigt averages of a polycrystal property are

derived [30]. They are represented in comparable stereographic projections using the same coloring levels as above (Fig. 10c and d). They clearly resemble the general pattern of the single crystal, rotated by  $45^\circ$  about the Z direction owing to the general preferred orientation of crystals, best described by a  $45^\circ$  rotated cube texture. Again, slight deviations from perfect symmetry correlate between the projections of Young's modulus and the corresponding pole figures of sample 10 (Figs. 7 and 8). About equally low minima of Young's modulus occur parallel to the building direction Z and parallel to the diagonal directions  $X \pm Y$ ; about equally high maxima occur at about  $55^\circ$  between Z and X, repeated four times according to cubic crystal symmetry. The sample reference directions X and Y carry equally some intermediate value.

Profiles along great circles over the stereographic projections are shown to emphasize the directionally dependence of Young's modulus (Fig. 10e). The band between the lower and upper bound marks the expected range for this given texture type. It is complemented by the curve for an infinitely sharp texture with the same preferred orientation, thus a  $45^\circ$  rotated single crystal. Furthermore, lower and upper bounds are derived for an isotropic material possessing a uniform texture. The weaker the texture the wider the bounds are separated: no separation for the single crystal, widest for the isotropic material.

The few values of Young's modulus measured by tensile testing along specific directions (X, Y and Z) are indicated in Fig. 10e. They fit well into the range between the corresponding bounds, for SLM specimen parallel and perpendicular to the building direction Z as well as for cast material. The expected range given by bounds for the same and some other sample directions is added to Table 1 at the bottom. It is beyond this study to discuss in depth whether the real values are supposed to fall higher or lower within the range given by Reuss and Voigt bounds, as this issue would extend from the analysis of crystal orientations to the additional incorporation of grain shapes. Certainly, the SLM material possesses a remarkable grain shape anisotropy and preferential alignment of grain long axes parallel to the building direction Z (Figs. 1 and 3). However, the potential effect of grain shape on the elastic anisotropy is confined to lie within the Reuss and Voigt bounds, and thus it is small compared to the variation due to crystal preferred orientation alone. As the bounds become narrower with increasing texture sharpness, the effect of grain shape is further reduced for materials with sharper textures.

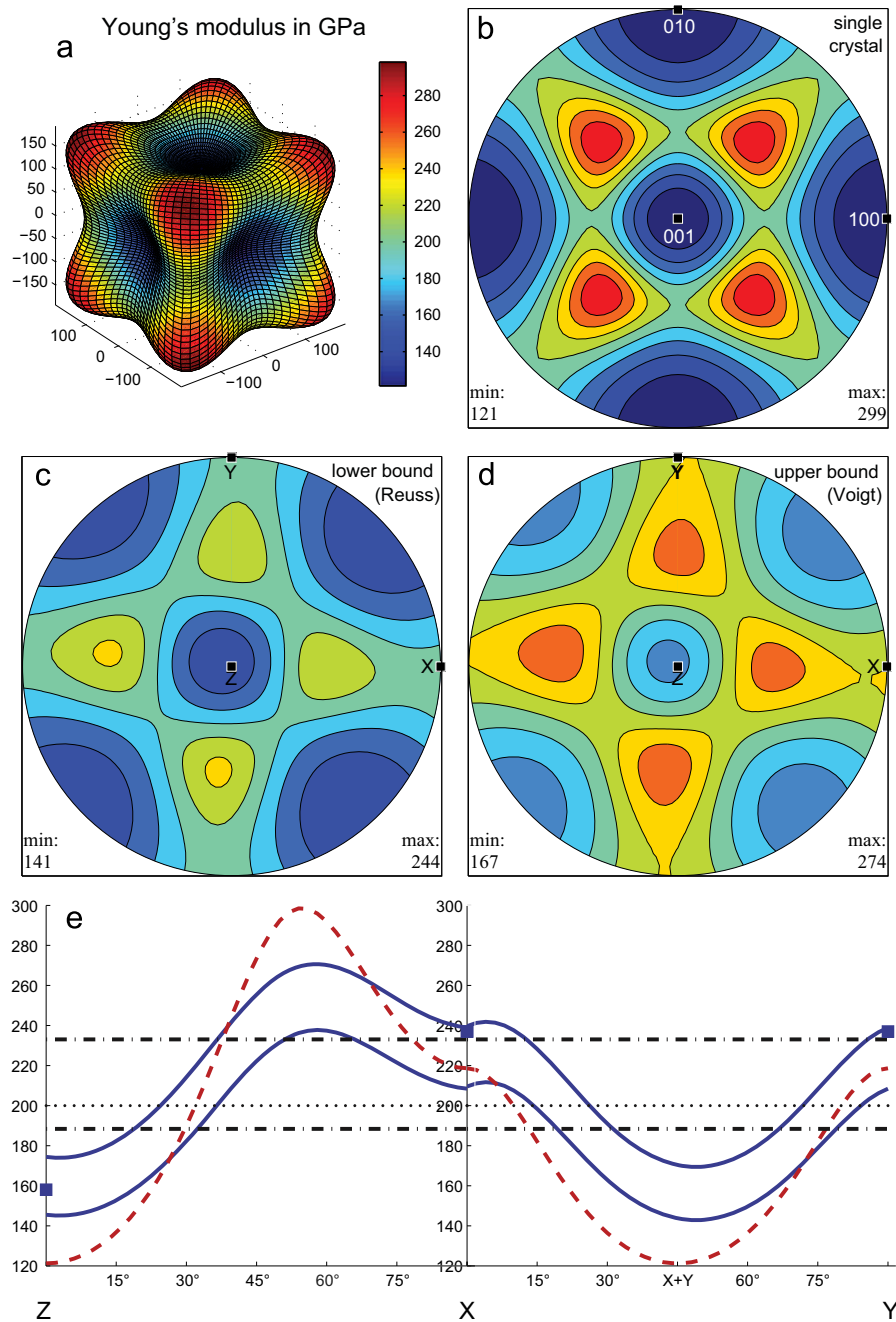


**Fig. 10.** Anisotropy in Young's modulus in SLM specimen. Same color legend applies from (a) to (d). (a) Single-crystal in three-dimensional visualization. (b) Single crystal in stereographic projection with respect to crystal axes. (c and d) Texture based lower/upper bound (Reuss and Voigt averages) in stereographic projection with respect to sample coordinates. (e) Profiles along great circles on the stereographic projections from Z via X to Y for lower and upper bounds (blue solid lines), for an infinitely sharp texture in the same principal orientation (red dashed line), for an isotropic material possessing uniform texture (black dash-dot lines). Measured values for SLM specimen (blue full squares) and isotropic reference value from database for cast material (black dotted line) are marked for comparison. (For interpretation of the references to color in this figure legend, the reader is referred to the web version of this article.)

From a point of tailoring material properties for applications, minimum Young's modulus can always be expected parallel to the building direction Z, but also along the laser scanning direction, here defined as the diagonal X+Y. A reasonable increase is already achieved when loading along the X or Y direction, while maximum Young's modulus is available along the directions between X and Z about  $55^\circ$  from Z. With suitable processing routes the SLM technique offers ways to take full advantage of the anisotropy by placing the critical component directions in an optimum way with respect to the building direction Z as well as with respect to the laser scanning direction in the XY-plane.

The elastic constants and therefore also Young's modulus typically reduce with increasing temperature. We have extrapolated the elastic constants of IN738LC to the testing temperature of  $850^\circ\text{C}$ , using temperature derivatives reported for Hastelloy X [31]. Applying these single crystal values (IN738LC at  $850^\circ\text{C}$ :  $c_{11}=193.49$  GPa,  $c_{12}=129.91$  GPa, and  $c_{44}=86.60$  GPa) and the same texture, the bounds for Young's modulus are calculated as well. The measured values at high temperature fall again within the estimated bounds. This approach presumes that the material does not go through any changes in crystal orientation nor in crystallographic phase over the investigated temperature range. The assumption is well acceptable, as

the material went through heat treatments at much higher temperatures (see top of Table 1) without significant changes observed in texture and microstructure.

Anisotropy of creep behavior in SLM specimens can be partly concluded from the directional variation of the Young's modulus and preferred orientation of the crystals. Another reason for improved creep behavior in Z-specimens is due to the application of the stress primarily parallel to the columnar elongated grains. In contrast, the load is applied mainly transverse to the grain boundaries in XY-specimens. It is well known that directionally solidified, columnar-grained, or single crystal superalloys have improved creep strength over conventionally cast material due to the fact that grain boundaries normal to the major stress axis are mostly eliminated [25].

The main reason for the inferior creep behavior of SLM specimens compared to cast material is most likely the significantly smaller grain size in SLM specimens, as shown by corresponding orientation maps (Figs. 2 and 4). Additional potential factors for differences in creep behavior are  $\gamma'$  precipitate size and morphology as well as decoration of grain boundaries with precipitates. As can be seen from Figs. 4 and 5, the carbide precipitates in heat-treated SLM specimens are significantly smaller and finer dispersed compared to the carbides in cast material.

In addition to tensile and creep testing, anisotropic material behavior is also expected for fatigue testing. Superior thermal fatigue resistance in Z-specimens compared to XY-specimens can be expected due to the lower Young's modulus in Z-specimens.

It is interesting to note that neither the grain size and morphology nor the texture of SLM specimens are affected by the applied heat treatment for several hours at maximum temperature of 1180 °C (details in Table 1). No indications are observed for recrystallization or grain coarsening, which is opposed to other reports on aging of SLM processed material [32,33]. Heat treatment trials for grain coarsening in SLM processed specimens are currently planned and will be reported later.

## 5. Conclusion

By using optimized SLM process parameters, crack-free parts of IN738LC with a macroscopic porosity below 0.5% can be manufactured, despite of the material's very poor weldability. The high cooling rates characteristic for the gas atomization in the SLM process suppresses diffusion-controlled processes, resulting in a very high chemical homogeneity and fine-grained columnar microstructure.

The characteristic layer-wise buildup of the SLM process leads to strong crystallographic preferred orientation (texture) in the materials, resulting in anisotropic properties of the produced IN738LC specimens. Specimens loaded within the XY-plane show inferior creep behavior compared to Z-specimens. The Young's modulus determined during tensile testing is significantly lower parallel to the building direction than perpendicular to the building direction, with the values for cast IN738LC material in between. Minimum Young's modulus can always be expected parallel to the building direction Z, but also along the laser scanning direction. Therefore both the building orientation and the laser scanning direction are crucial for the mechanical integrity of a part. This adds a new dimension of complexity to the optimal processing protocol for parts of complicated shape. Spatial and temporal variation of scanning patterns during the process should be employed for optimum texture and properties. Even further, if processing steps can be performed with gradual

variation of these reference directions in sequence, gradients of mechanical properties can be expected to be achievable. The choice of scanning strategy is no more influenced by geometrical and cost factors alone but also by material property requirements appropriate for the specific application.

## Acknowledgments

Authors are indebted to Lukas Rickenbacher (ALSTOM Switzerland) for processing of SLM specimens and to Dr. Erik Reusser (Earth Science Department of ETH Zürich) for electron probe microanalysis. Comments by an anonymous reviewer are gratefully acknowledged.

## References

- [1] M. Durand-Charre, J.H. Davidson, *The Microstructure of Superalloys*, Gordon and Breach Science Publ., Amsterdam, 1997 124 pp.
- [2] C.T. Sims, *Superalloys II [High-Temperature Materials for Aerospace and Industrial Power]*, Wiley, New York, N.Y. (1987) 615 pp.
- [3] C. Hays, *J. Mater. Eng. Perform.* 17 (2) (2008) 254–259.
- [4] E. Balıkcı, R.A. Mirshams, A. Raman, *J. Mater. Eng. Perform.* 9 (3) (2000) 324–329.
- [5] E. Balıkcı, A. Raman, R.A. Mirshams, *Metall. Mater. Trans. A—Phys. Metall. Mater. Sci.* 28 (10) (1997) 1993–2003.
- [6] S. Behrouzghaemi, R.J. Mitchell, *Mater. Sci. Eng. A—Struct. Mater. Prop. Microstruct. Process.* 498 (1–2) (2008) 266–271.
- [7] O.A. Ojo, M.C. Chaturvedi, *Mater. Sci. Eng. A—Struct. Mater. Prop. Microstruct. Process.* 403 (1–2) (2005) 77–86.
- [8] O.A. Ojo, M.C. Chaturvedi, *Metall. Mater. Trans. A—Phys. Metall. Mater. Sci.* 38A (2) (2007) 356–369.
- [9] N.A. Ojo, N.L. Richards, M.C. Chaturvedi, *J. Mater. Sci.* 39 (24) (2004) 7401–7404.
- [10] O.A. Ojo, N.L. Richards, M.C. Chaturvedi, *Scr. Mater.* 51 (2) (2004) 141–146.
- [11] O.A. Ojo, N.L. Richards, M.C. Chaturvedi, *Metall. Mater. Trans. A—Phys. Metall. Mater. Sci.* 37A (2) (2006) 421–433.
- [12] M. Rombouts, et al., *CIRP Ann.—Manuf. Technol.* 55 (1) (2006) 187–192.
- [13] S. Das, et al., *Mater. Des.* 21 (2) (2000) 63–73.
- [14] F.D.S. Marquis, and Minerals Metals & Materials Society (Warrendale PA) Powder Materials Committee, Rapid prototyping of materials proceedings of symposium... held October 7–10, 2002, at the Crown Plaza Hotel in Columbus, Ohio, USA, 2002, Warrendale, Pa.: TMS, 224 pp.
- [15] L. Rickenbacher, et al., *Rapid Prototyp. J.* 19 (4) (2013) 282–290.
- [16] F. Wang, *Int. J. Adv. Manuf. Technol.* 58 (5–8) (2012) 545–551.
- [17] Z.M. Wang, et al., *J. Alloys Compd.* 513 (2012) 518–523.
- [18] K.A. Mumtaz, P. Erasenthiran, N. Hopkinson, *J. Mater. Process. Technol.* 195 (1–3) (2008) 77–87.
- [19] L.N. Carter, M.M. Attallah, R.C. Reed, in: Eric S. Huron, Roger C. Reed, Mark C. Hardy, Michael J. Mills, Rick E. Montero, Pedro D. Portella, Jack Telesman (Eds.), *Superalloys 2012*, John Wiley & Sons, Inc., 2012, pp. 577–586.
- [20] L. Thijs, et al., *Acta Mater.* 61 (5) (2013) 1809–1819.
- [21] U.F. Kocks, et al., *Texture and Anisotropy Preferred Orientations in Polycrystals and Their Effect on Materials Properties*, Cambridge University Press, Cambridge (1998) 676 pp.
- [22] J. Niehuesbernd, et al., *Mater. Sci. Eng. A—Struct. Mater. Prop. Microstruct. Process.* 560 (2013) 273–277.
- [23] R. Hielscher, H. Schaeben, *J. Appl. Crystallogr.* 41 (2008) 1024–1037.
- [24] F. Bachmann, R. Hielscher, H. Schaeben, *Solid State Phenom.* 160 (2010) 63–68.
- [25] T. Abbas, F.A. Khawaja, *Solid State Commun.* 49 (7) (1984) 641–644.
- [26] A.K. Jena, M.C. Chaturvedi, *J. Mater. Sci.* 19 (10) (1984) 3121–3139.
- [27] E. Balıkcı, R.E. Ferrell, A. Raman, *Z. Metallkunde* 90 (2) (1999) 141–146.
- [28] D.A. Porter, K.E. Easterling, M.Y. Sherif, *Phase Transformations in Metals and Alloys*, 3rd ed., CRC Press, Boca Raton, FL (2009) 520 pp.
- [29] J.B. Han, et al., *Mater. Sci. Eng. A—Struct. Mater. Prop. Microstruct. Process.* 191 (1–2) (1995) 105–111.
- [30] D. Mainprice, R. Hielscher, H. Schaeben, *Deformation Mechanisms, Rheology and Tectonics: Microstructures, Mechanics and Anisotropy*, in: D.J. Prior, E.H. Rutter, D.J. Tatham (Eds.), *Geological Society, London*, 2011, pp. 175–192.
- [31] H.A. Canistraro, et al., *J. Eng. Mater. Technol.—Trans. ASME* 120 (3) (1998) 242–247.
- [32] P. Kanagarajah, et al., *Mater. Sci. Eng. A—Struct. Mater. Prop. Microstruct. Process.* 588 (2013) 188–195.
- [33] F.C. Liu, et al., *Opt. Laser Technol.* 43 (1) (2011) 208–213.